Experiments in Fluids (2023) 64:196
https://doi.org/10.1007/s00348-023-03733-5

RESEARCH ARTICLE

Imaging of flame propagation and temperature distribution in an all-metal gasoline engine with endoscopic access via anisole fluorescence

Muhammad Ali Shahbaz[1,2] · Saad Jahangir[2] · Sebastian A. Kaiser[1]

Received: 3 July 2023 / Revised: 27 September 2023 / Accepted: 21 October 2023 / Published online: 7 December 2023

Abstract

Laser-based optical diagnostic tools are widely used to investigate in-cylinder processes in internal combustion engines. For laser-induced fluorescence (LIF), many tracers have been used in the past. Recently, anisole has been characterized spectroscopically for engine-relevant pressures and temperatures and emerged as a potentially advantageous alternative to more commonly used tracers in the past due to its photo-physical properties. Its high fluorescence quantum yield and large absorption cross section result in high signal intensity. This is particularly beneficial for endoscopic imaging systems, which typically have worse light collection efficiency than traditional imaging systems in fully optically accessible engines with transparent liners. In this work, we exploited the strong anisole LIF signal in two single-shot experiments: to image flame propagation, and the instantaneous gas-phase temperature during compression stroke and gas exchange process. Measurements were performed in a production gasoline engine modified for endoscopic optical access via an advanced UV endoscope system. First, LIF of anisole was compared to that of toluene during compression stroke. Anisole LIF yields a much higher signal-to-noise ratio and better image quality with lower tracer concentrations. Due to the higher signal of anisole LIF, small structures of the turbulent flame burning into the anisole/isooctane mixture were well visible after ignition. Second, the red-shift of the anisole fluorescence spectrum with increasing temperature and oxygen partial pressure was exploited for ratiometric temperature measurements based on single-shot images. The available spectroscopic data were used to develop several signal ratio models, which were calibrated in situ using a heated tracer/bath gas mixture introduced inside the combustion chamber. The calibrated signal ratio models were then extrapolated to the engine-relevant ranges. Models with two-step exponential interpolation show better agreement with the adiabatic temperature than linear or 3D surface exponential interpolation. The gas-phase temperature images based on single shots were obtained using one selected model, showing a near uniform and a stratified temperature distribution during the compression stroke and gas exchange process, respectively.

Abbreviations

ºCA	Degree crank angle
BP	Band pass (filter)
DC	Direct current
DISI	Direct-injection spark ignition
ECU	Engine control unit
FOV	Field of view
IC	Internal combustion
ICCD	Intensified charge couple device
Imep	Indicated mean effective pressure
IVC	Intake valve close
LIF	Laser-induced fluorescence
LIF	Laser-induced fluorescence
LP	Low pass (filter)
Nd:YAG	Neodymium-doped yttrium aluminum garnet
PFI	Port fuel injection
p_{O2}	Oxygen partial pressure
ROI	Region of interest
SLIPI	Structured laser illumination planar imaging
SNR	Signal-to-noise ratio
TDC	Top dead center
UV	Ultraviolet

✉ Sebastian A. Kaiser
sebastian.kaiser@uni-due.de

Muhammad Ali Shahbaz
alishahbaz@uet.edu.pk

[1] Institute for Combustion and Gas Dynamics - Reactive Fluids, University of Duisburg-Essen, 47057 Duisburg, Germany

[2] Automotive Engineering Centre, University of Engineering and Technology, Lahore, Pakistan

1 Introduction

Optical diagnostics are fast and non-intrusive tools used to investigate in-cylinder processes in internal combustion (IC) engines in high temporal and spatial resolution. These are typically applied on single-cylinder "optical" engines with transparent liners and pistons. These optical engines have an advantage of large optical access, but the thermodynamic properties and speed/load range are different from those of all-metal engines. To apply optical diagnostics in more realistic environment, minimally invasive endoscopes are used in all-metal engines. These "endoscopic" engines have the advantage of having nearly unmodified thermodynamic properties and speed/load range as the production engines. Different endoscopes have been used in the past to visualize various in-cylinder phenomena. Most of the endoscopes used are only transparent in the visible range and have poor light collection efficiency. Richter et al. compared a standard Karl Storz endoscope with widely available UV-Nikkor *f*/4.5 lens and found the collection efficiency of Karl Storz endoscope to be 30 times worse (Richter et al. 1998). Therefore, the application of such endoscopes is limited to relatively bright events in the visible range only. Few examples are visualization of broadband combustion in gasoline (Drake et al. 2003; Fach et al. 2022) and in diesel engines (Eismark et al. 2009; Miers et al. 2005), temporally resolved soot pyrometry (Bakenhus and R. D. Reitz 1999; Shiozaki et al. 1996), visualization of the spray via Mie scattering (Sczomak et al. 2010; Sementa et al. 2012; Fach et al. 2021), and particle image velocimetry (PIV) (Fach et al. 2021, 2022; Dierksheide et al. 2002). Soot formation has also been investigated using endoscopic imaging in direct-injection spark-ignition (DISI) engines by Burkardt et al. (2021) and Etikyala et al. (2022). To apply a wider range of optical diagnostics in engines with endoscopic access, in our previous work, a large-aperture hybrid UV-transparent endoscope system was developed (Reichle et al. 2012; Zimmermann 2006). It is now commercially available from LaVision. Other versions of UV-transparent endoscopes are used to investigate the combustion in hydrogen-fueled engines by imaging OH radical in Eicheldinger et al. (2021) and Karmann et al. (2022).

Tracer-based laser-induced fluorescence (LIF) is a widely used optical diagnostic tool for quantitative measurement of fuel concentration, temperature, and fuel/air ratio in combustion applications (Schulz and Sick 2005; Deguchi et al. 2002; Kuwahara and Ando 2000). LIF has also been used to detect the flame front via the "negative-LIF" technique (Bladh et al. 2005; Attar et al. 2015) (i.e., the disappearance of the tracer where the fuel is burned), to investigate the spray in a diesel marine engine (Hult and Mayer 2013) and formation and evaporation of piston fuel films (Alger et al. 2001; Geiler et al. 2017; Hochgreb 2001). Previously, toluene (methylbenzene, $CH_3C_6H_5$, boiling point 111 °C) has been well investigated as a tracer for LIF applications (Düwel et al. 2003; Faust 2013; Koban et al. 2005) and used for measurements in combustion engines, e.g., to image equivalence ratio and fuel distribution (Frieden and Sick 2003; Smith and Sick 2005; James and Smith 2005), to investigate fuel films in DISI engines (Geiler et al. 2017; Schulz and Beyrau 2018; Schulz et al. 2016), and to image the gas-phase temperature distribution via the ratio in single (Fuyuto et al. 2006) and two spectral bands (Gessenhardt et al. 2015; Luong et al. 2008; Peterson et al. 2013). Since toluene is a component of typical commercial gasoline, pure toluene has also been used as a surrogate fuel for LIF applications in combustion engines (Warey et al. 2002). More recently, anisole (methoxybenzene, $CH_3OC_6H_5$, boiling point 154 °C) was characterized spectroscopically for engine-relevant pressures and temperatures (Tran et al. 2013; Benzler 2019; Faust et al. 2013; Zabeti et al. 2017) and emerged as a potentially advantageous alternative to toluene (Faust 2013; Benzler 2019; Faust et al. 2014). The effect of tracer quantity added into the non-fluorescent base fuel can generate a substantial systematic error due to their differences in physical properties, and hence prevent the accurate quantification of LIF signals (Schulz and Sick 2005). The absorption cross section of anisole, when excited at 300 K with 266 nm laser radiation, is about 50 times larger and the fluorescence quantum yield is 63% larger than that of toluene (Faust et al. 2013). Therefore, anisole produces a stronger LIF signal per volume than toluene, which may enable better measurements, with less effect on the combustion process due to the lower tracer concentration required.

Like most aromatic species, the fluorescence of both toluene and anisole shows a red-shift with increasing temperature. This can be exploited to measure temperature by using two-color LIF thermometry. In this technique, the LIF signals are measured in two spectrally distinct regions (namely red and blue channels for shorter and longer wavelength bands, respectively). Due to the red-shift of LIF spectra with the increase in temperature, accompanied by an increase in the spectral width, relative signals increase in the red channel and decrease in the blue. The signal intensities detected in each channel, resulting from the combination of the temperature-dependent LIF spectra with the respective wavelength-dependent detection quantum efficiency, yield a signal ratio that can be used to determine the temperature. Since the measurement is based on taking the ratio between two spectral bands, it is very sensitive to the noise that accompanies low fluorescence signals (Peterson et al. 2014). In this work, it was investigated if

the previously reported endoscopic two-color LIF thermometry (Gessenhardt et al. 2015) could be improved to single-shot imaging by substituting anisole for toluene. In addition to the (desired) red-shift of the fluorescence spectra with increasing temperature, anisole also has an undesired, but lesser, red-shift with increasing oxygen partial pressure (p_{O2}) that needs to be considered. The effect of p_{O2} is more pronounced at pressures lower than what corresponds to atmospheric pressure, i.e., 210 mbar p_{O2} (Faust et al. 2013), which is relevant to the in-cylinder conditions in the intake stroke. Even though toluene has no p_{O2}-dependent red-shift when excited with 266 nm laser (Koban et al. 2005) which makes it more convenient to use as a tracer in two-color LIF thermometry technique, the stronger LIF signal of anisole fluorescence spectra make the latter more advantageous for single-shot temperature measurements. The temperature and p_{O2} dependence of the anisole LIF spectra was considered in a spectroscopic model for determining the gas-phase temperature from the pixel-wise red/blue signal ratio and p_{O2}, the latter determined from the in-cylinder pressure data. This theoretical spectroscopic model was then calibrated in situ. A simple calibration equipment was designed and used to perform in situ calibrations over a broad range of temperatures with air and nitrogen as bath gases. Different mathematical interpolation models were then used to extend the range of the spectroscopic models. These models were then used to determine temperatures along the compression stroke, and the results were compared to the adiabatic-core temperature. Finally, a selected model was used to visualize the temperature distribution during the compression stroke, and temperature stratification and mixing of fresh charge and internally recirculated exhaust gas during the gas exchange process.

2 Engine and optics

Measurements were performed in a production line, four-cylinder, inline, naturally aspirated, spark-ignited engine (BMW N46 B20). The engine operated with stoichiometric fuel/air ratio and was equipped with port fuel injection (PFI) and a mechanically actuated variable intake valve train (Valvetronic). The engine was coupled to a speed-controlled dynamometer, with the torque controlled by an analog input to the engine control unit (ECU). Actuators, valve lift and timing, phasing and injection were managed by the production ECU accordingly, to which there was read-out access only. The engine geometry and operating parameters are given in Table 1.

The engine is modified in the fourth cylinder (the one nearest to the flywheel) to have two mutually perpendicular small endoscopic ports of 13 mm diameter each, one for illumination and other for detection. More details about the engine and the modifications for endoscopic accesses can be found in Gessenhardt (2013) and Witzel (2007). The hybrid UV endoscope system consists of two parts: a wide-angle front endoscope and a refractive-diffractive ("hybrid") relay lens for chromatic correction in a pre-designed range (Reichle et al. 2012; Zimmermann 2006). The front endoscope is mounted on the engine and produces an intermediate image on the field lens at its back. This intermediate image is passed onto the hybrid relay lens without a rigid physical connection and projected onto a camera. The detection hardware (filters, relay lenses, and cameras) is mounted on a separate rigid frame. The absence of a rigid connection between the engine and the detection hardware (see Fig. 1) makes the latter isolated from engine vibrations. Moreover, filters and other optical elements can be placed between the front endoscope and the hybrid relay lens. The field of view (FOV) is approx. 30×30 mm^2 area at a distance of 35 mm (Reichle et al. 2012).

Table 1 Engine geometry and operating parameters

Displacement volume	1995 cm^3
Bore	84.0 mm
Stroke	90.0 mm
Compression ratio	10.0: 1
Number of valves per cylinder	4
Engine speed	2000 revolutions min^{-1}
Indicated mean effective pressure	4 bar
Intake valve lift	2.2 mm
Exhaust valve lift	9.7 mm
Fuel	Isooctane (C_8H_{18}) with 20% toluene or 2.5% anisole
Equivalence ratio	1.0

A custom fuel supply allowed "clean" operation on neat surrogate fuels without unknown fluorescing compounds in the endoscopically accessed cylinder, while a commercial fuel pump supplied high-octane commercial fuel to the other cylinders. All measurements were performed in continuously fired operation at 2000 min^{-1} and 4 bar indicated mean effective pressure (imep). Throttling to this part load was achieved by an intake valve lift of 2.2 mm. Ignition occurred at -35 °CA. (0 °CA is compression top-dead center, i.e., crank angles during intake and compression are negative). On the endoscopically accessed cylinder, the crank angle resolved pressure was measured and recorded. The temperatures of the intake and exhaust gases, engine oil, and cooling water during the measurements are given in Table 2. The cameras and laser were controlled and synchronized with the engine by DaVis (version 8): imaging software from LaVision.

A schematic of the optical geometry of the modified cylinder, camera, and laser guiding arm is shown in Fig. 1. The dashed boxes represent two independent and rigid frames. The beam of an Nd:YAG laser at 266 nm with a maximum

Table 2 Air, water, and engine oil temperatures measured during the experiment

	Temperature [K]
Intake air	308
Exhaust gases	880
Engine oil	390
Cooling water inlet	298
Cooling water outlet	380

repetition rate of 10 Hz was introduced into the light sheet endoscope via a laser guiding arm. The laser energy was 2 mJ/pulse as measured before the endoscope that generated a 0.5 mm thick, vertically diverging laser light sheet through a set of cylindrical optics. A long-pass filter (LP 266) mounted behind the detection endoscope blocked reflected laser light. A beam splitter (LP 310) transmitted light above 310 nm onto a 12-bit ICCD (max counts: 4096) yielding an image from the "red" part of the LIF spectrum, while the reflected light below 310 nm was detected by an identical camera in the "blue" channel. The linear bias in measured signal ratio due to the angular dependence of the transmission spectrum of beam splitter, as considered in Peterson et al. (2014), was not considered in this case because the light coming from the field lens was near-parallel (Shahbaz et al. 2023) (The change in incidence angle is only 0.44% from the parallel beam). Band-pass filters further constrained the spectral range of each "color" channel (BP 320/40 for the red channel and BP 280/20 for the blue channel). Both cameras were gated for 200 ns bracketing the laser pulse.

Figure 2 gives an overview of the most important spectral features in emission and detection. As the fluorescence spectra red-shift with increasing temperature, as shown in Fig. 2, the ratio of the signals detected on each camera changes. This ratio can be related to local temperature by a suitable calibration.

Based on our previous work on two-color tracer-LIF (Gessenhardt et al. 2015), 20% toluene by volume was added in isooctane base fuel. For experiments with anisole as the tracer, only 2.5% anisole was added to the isooctane base fuel to keep the absorption of the laser beam across the field of view similar.

3 Signal model for temperature measurements

3.1 Spectroscopic signal ratio model

Figure 3 shows measured peak-normalized anisole LIF spectra, shifting toward longer wavelengths (red-shift) with an

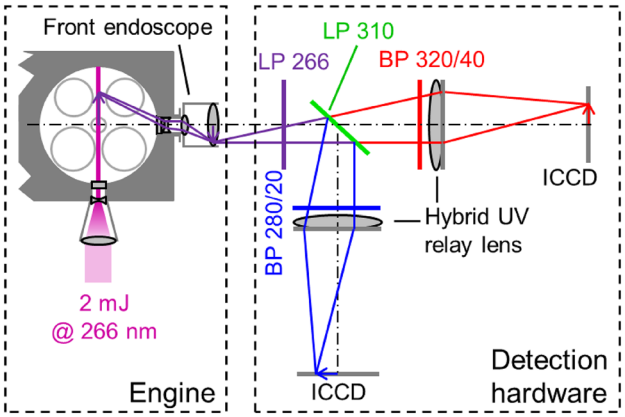

Fig. 1 A schematic of engine, optics, and detectors

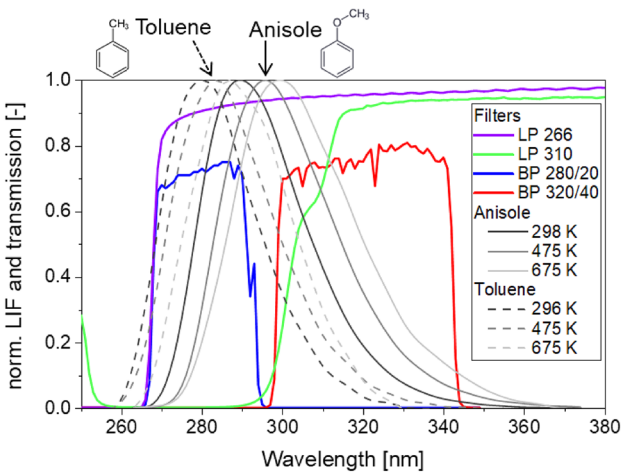

Fig. 2 Spectral overview of emission and detection. Toluene and anisole LIF at different temperatures, and transmission of the filters used for two-color detection. Anisole and toluene spectra are from (Faust 2013)

increase in temperature and p_{O2} (data taken from Faust et al. (2013)). The 'red' and 'blue' spectral regions that are used to determine the signal ratio are highlighted. The temperature dependence of red-shift due to increase in p_{O2} (Fig. 3b) is within the experimental error up to temperatures of 600 K (Faust et al. 2013) and therefore neglected.

The change in the red/blue signal ratio with temperature and p_{O2} was determined by first estimating the expected LIF signals in each channel at different temperatures and p_{O2}. The wavelength-dependent quantum efficiency of each detection channel, which includes the transmissivity of the sapphire window and quartz lenses in the front endoscope, spectral response of the beam splitter to different wavelengths, the transmissivity of band pass filters, as well as intensifier's quantum efficiency, was considered, while the intensifier gain was assumed constant for both channels.

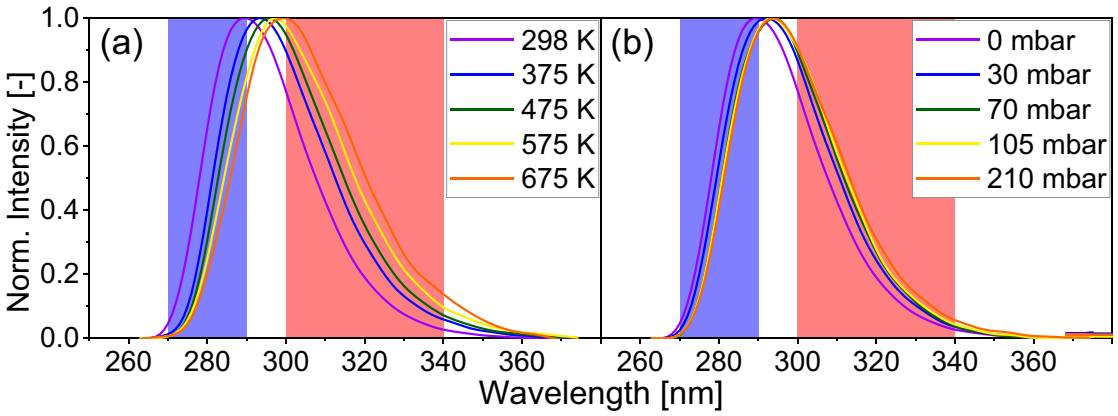

Fig. 3 **a** Spectral shift of anisole spectra with temperature (in nitrogen) and **b** with p_{O2} (at 296 K). Spectral data from (Faust et al. 2013)

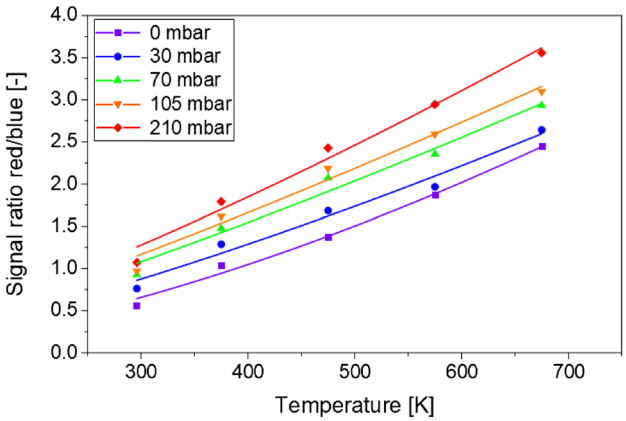

Fig. 4 Spectroscopic signal ratio model from measured anisole LIF spectra at different p_{O2} and temperatures (Faust et al. 2013)

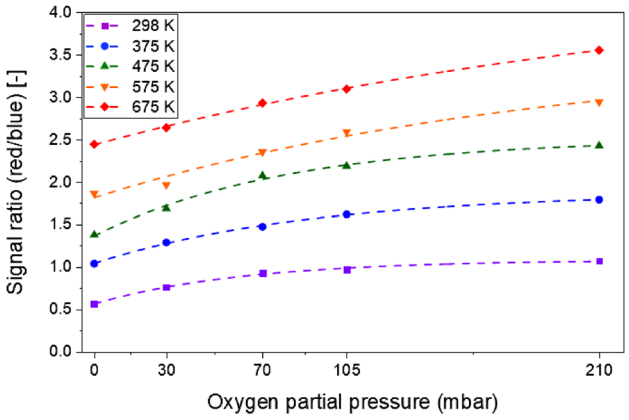

Fig. 5 Effect of p_{O2} on the signal ratio at different temperatures

Figure 4 shows the signal ratios estimated by spectral integration of the anisole spectra at five temperatures and five p_{O2}. The discrete data points were fitted with the exponential function:

$$\mathrm{SR} = ay^b, \tag{1}$$

where SR is the signal ratio, y is temperature [K], and a and b are constants.

Figure 5 shows how the signal ratio (red/blue) is affected by p_{O2}. The data points here are the same signal ratios as in Fig. 4, now plotted versus p_{O2}. The dashed lines represent the exponential fit function:

$$\mathrm{SR} = a + be^{cx}, \tag{2}$$

where x is p_{O2} [mbar], and a, b, and c are constants.

Figure 5 shows that the effect of p_{O2} is stronger at lower p_{O2} and lessens with the increase in p_{O2}. However, at the higher temperatures, the saturation point of the curve is at higher p_{O2}, as can be seen by the slope at the end of the fitted curve at 675 K. During compression, both temperature and pressure and thus p_{O2} increase. In a spark-ignition engine, we may expect at least 800 K and a few bar p_{O2} toward the end of compression. Unfortunately, in particular for p_{O2}, the range of the literature data is narrow, and some extrapolation will be needed, as discussed below.

3.2 In situ calibration

An in situ calibration was performed since the signal ratios estimated at different temperatures and p_{O2} are based on assumptions that might change during actual experiments. This includes the angle of the beam splitter, similar response of both intensifiers at similar gain value, similar noise in both intensifiers and nonlinearities in the intensifiers. In situ calibration measurements in the engine were performed at different temperatures, ranging from 300 to 570 K, with anisole seeded into two bath gases, air or nitrogen, i.e., 210 and 0 mbar p_{O2}, respectively. The liquid anisole was evaporated

into the bath gas in a bubbler. This gas was then passed through a heated quartz tube with an exit diameter of 7 mm into the combustion chamber via the spark plug bore. The bath gas temperature was measured by a thermocouple 5 mm downstream of the tube exit and was controlled by varying the voltage supplied to the heater. The gases were supplied at a pressure of 1 bar and a flow rate of 0.3 L/s. Higher absolute pressures were not used to avoid generation of the shock waves upon sudden release into the atmosphere.

Imaging the jet that issued from the heated tube into the cylinder, we found that the background varied in intensity from shot to shot, presumably due to scattering and reflections. To account for this, a dynamic background subtraction strategy was used. The laser beam was shaped into five sub-beams, each with a diameter of about 0.5 mm as shown in Fig. 6, an example image from the blue channel taken at 473 K. The black box represents the region of interest (ROI) for averaging the signal and the red box for the background. The signal intensity around the black box is less than the rest of the beam due to higher temperature of the jet coming out of the heated nozzle. Intake and exhaust sides are marked by IV (intake valve) and EV (exhaust valve), respectively.

To ensure that the tracer/bath gas mixture was at a stable temperature at ROI, the tracer/bath gas mixture was allowed to flow for approximately 1 min at a steady temperature before recording the images. Three measurements were performed with each bath gas, and unseeded bath gas was allowed to flow through the combustion chamber between each measurement for at least 30 min to ensure complete flushing and cooling of the cylinder. For the measurements with nitrogen as bath gas, the combustion chamber was additionally flushed with nitrogen to completely remove the air, which would otherwise interfere

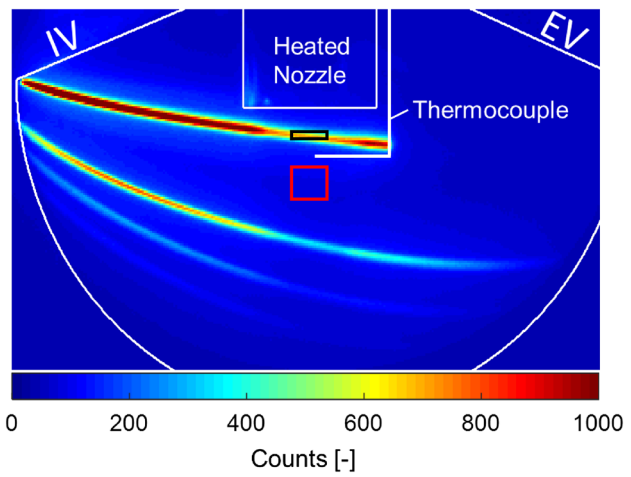

Fig. 6 Blue channel image from the calibration measurement at 473 K. IV and EV are intake and exhaust valves, respectively. The black box shows the ROI for the signal and the red box shows the ROI for dynamic background

with the results due to presence of oxygen. Care was taken to keep the optical setup the same for the calibration measurements and the engine runs. The measurements were performed with both increasing and decreasing temperature, and the values of signal ratios at each temperature were averaged.

In another experiment, the effect of intensifier gain on the signal ratio was investigated. It was found that the quantum efficiency of the intensifier at different values of gain is not the same, and thus, the signal ratio changed, apparently linearly, with a change in gain value. Further details can be found in Shahbaz (2021). This is important since the calibration measurements and the measurements in the running engine are performed at different gain values. The calibration data were adjusted accordingly to compensate for the difference in gain values.

A calibration function was found by trial and error considering different pre-factors and orders of dependencies. The final ad hoc calibration function is a combination of a constant offset, a second-order dependency on the signal ratio, and a first-order dependency on the product of signal ratio and temperature and is given as:

$$SR_{calibrated} = 0.44 + 0.16 \cdot SR - 0.039 \cdot SR^2 + 0.000705 \cdot SR \cdot T, \quad (3)$$

where SR is uncalibrated signal ratio and T is temperature [K].

A detailed description of the complete calibration process is reported in Shahbaz (2021). The signal model obtained from spectroscopic data and the calibrated signal model after applying the calibration function are shown in Fig. 7a and b, respectively. The signal ratios are fitted with the exponential function given by equation (1). The exponential fit functions, based on equation (1), obtained from the signal ratios in the calibration measurements in air and nitrogen are shown as black lines encompassing the calibrated signal model. The slope of the calibrated fits is significantly lower than that derived from the spectroscopic data only, i.e., the actual measurement is less sensitive to temperature.

The calibration data as shown in Fig. 7b are limited to 210 mbar p_{O2} and a temperature of 675 K, whereas in the measurements in the running engine, the p_{O2} is as high as 3 bar and the temperature up to 1000 K. Therefore, the calibrated model was extrapolated using two different strategies which are described in the following section. The values of constants for equation (1) and equation (2) for the in situ calibrated data points, as shown in Fig. 7b, are given in Appendix 1 and Appendix 2, respectively, in the supplementary material.

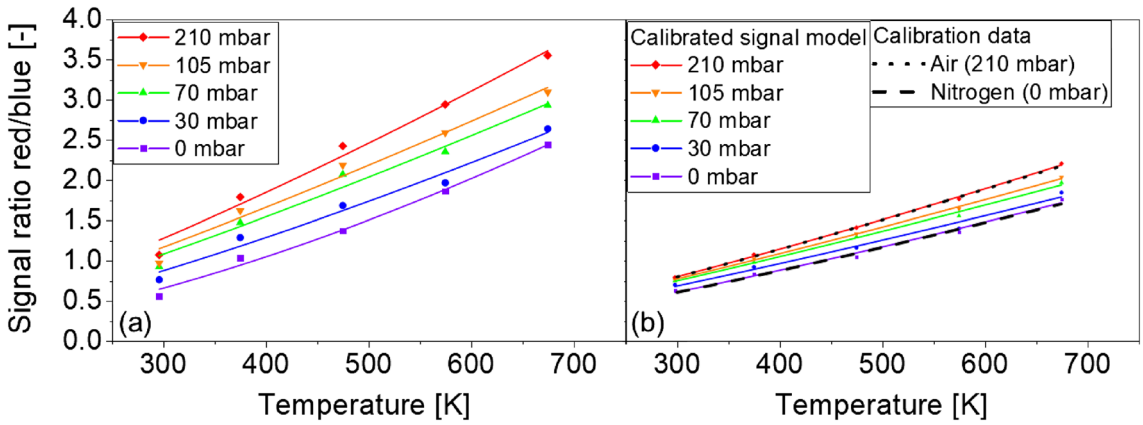

Fig. 7 Calibration of the signal model. **a** Signal model from the spectroscopic data. **b** Calibrated signal model and calibration data

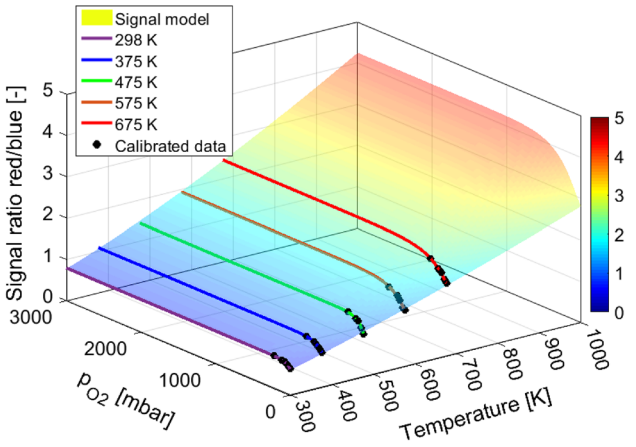

Fig. 8 Effect of temperature and p_{O2} on signal ratio based on two-step extrapolation with two-parameter exponential temperature-dependent function as given in equation (1)

3.3 Two-step fit

Figure 8 shows the extrapolated signal model using the two-step fit strategy. The black points show the calibrated signal ratios. First, five fit functions (based on equation (2)) were extracted for the calibrated signal ratios and used to generate a discretized data set of signal ratios up to 3000 mbar p_{O2} at five temperatures, with increments of 1 mbar (shown by colored lines in Fig. 8). In the second step, a fit function, as given in equation (1), was determined for any given value of p_{O2}. The values for the coefficients of this fit function were different for every value of p_{O2} and were just used to calculate the temperature and were not stored. To determine the temperature, the equation of the fit function in equation (1) was rearranged to determine the temperature from the signal ratio at a given p_{O2}. To visualize the signal model, the fit functions for each value of p_{O2} are plotted up to a temperature of 1000 K in steps of 10 K and are shown in Fig. 8. The extrapolated range for p_{O2} is approximately 14 times wider than that of the available data.

In order to compare different approaches in two-step fit strategy, the two-parameter temperature-dependent exponential function in equation (1) was replaced by a linear function, and alternatively a three-parameter exponential function as used by Kranz et al. (2018). The signal models using these two functions are shown in Appendix 4 and Appendix 5 in the supplementary material, respectively. Detailed discussion is available in Shahbaz (2021).

3.4 3D surface fit

In this strategy, a single surface fit function was determined instead of two separate functions for temperature and p_{O2}. The equation for the surface fit was formulated by combining equations (2) and (1) and is shown as:

$$SR = (a + b \cdot e^{cx}) \cdot (dy^{f}), \tag{4}$$

where *a, b, c, d,* and *f* are constants (given in Appendix 3 in the supplementary material). The first part of the equation (4) is p_{O2} and the second is temperature-dependent.

Figure 9 shows the resulting surface evaluated over the same range as in Fig. 8. Since the temperature exponent is nearly unity (see Appendix 3 in the supplementary material), the signal ratio does not increase exponentially as it does with the two-step fit strategy. The temperature was determined simply by rearranging equation (4) for a given value of p_{O2} and signal ratio. For comparison, the temperature-dependent part of equation (4) was replaced by a linear function and used to calculate the temperature. A linear temperature-dependent function resulted in a very similar surface as in Fig. 9, and is therefore not shown here. For any given value of signal ratio, the two-step and 3D surface

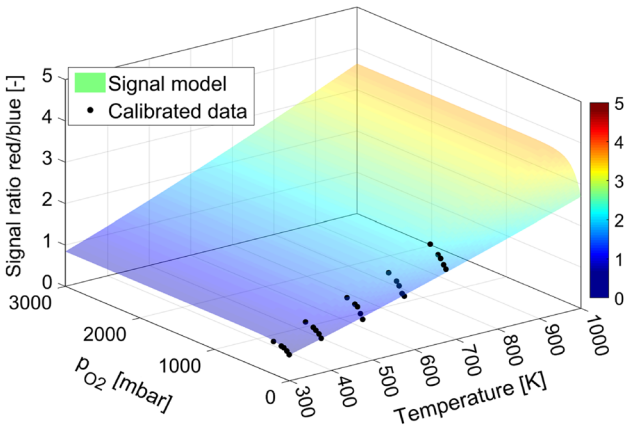

Fig. 9 Extrapolated 3D surface fit based on equation (4)

fit models described above give different values of temperatures at higher p_{O2} values (corresponding to crank angles later in the compression stroke). This is explained later in the results section.

4 Images and post-processing

Figure 10 shows the image post-processing steps for extracting the signal ratios for each image at a crank angle. The images were first coarsely registered (mapped onto each other) in DaVis with a UV-illuminated target mounted on the detection endoscope in place of the field lens, and then more precisely based on actual LIF images in MATLAB R2017a (The MathWorks Inc., Natick, USA). After registration, the regions outside the FOV and, where applicable, those blocked by the piston are masked out. The dynamic background (BG) was then subtracted from each image by averaging a 30 × 100 pixel area from the shadowed region by the spark plug's ground electrode (shown as red rectangle in Fig. 10 (1)).

Next, as shown in Fig. 10 (3–5), the 'burnt area' where the signal is only background was masked out at later crank angles. To achieve this, a flat field was obtained by averaging 100 images obtained at each crank angle from the same experiment under fired conditions. The flat-field images were homogeneous during most of the compression stroke, i.e., before ignition at − 35 °CA bTDC. However, after ignition the fluctuating location of the flame starts affecting the homogeneity of flat-field image. For the images where the flame kernel was small (i.e., − 20 °CA bTDC), the effect was limited to the regions close to the spark plug. However, for the later crank angles where the flame front was larger and fluctuating, the effect was not negligible. However, since it was not possible to obtain a flat-field image with unfired operation on the test bench, the images obtained under the fired operation were used to obtain flat field. The flat field obtained at later crank angles under fired conditions still yielded sufficient correction for successful binarizing by thresholding. The single-shot images were divided by this flat-field image. If this flat-field correction is not performed, binarizing by simple thresholding would also eliminate some 'useful' regions on the right side of the image that have lower signal due to laser absorption. The flat-field corrected images were then smoothened by a 5 × 5 mean filter, normalized by the maximum count value and binarized by thresholding at 18% of that maximum count value. This binarizing process eliminated all of the burnt gas and unilluminated regions.

In the next step, the binary image was then multiplied with the background-corrected images in both channels and 3 × 3 mean filtering was applied to reduce the noise (Fig. 10 (6)). The image from the red channel was divided pixel-wise by the image from the blue channel to yield the signal ratio image. The average signal ratio was determined by averaging just the non-zero pixels in a 100 × 150 pixel ROI below the spark plug, as shown in Fig. 10 (7). If the nonzero pixels filled less than 25% of the ROI, as could be the case at later crank angles with larger burnt regions, the results were discarded. This resulted in 100 values for the signal ratio at crank angles before and just after ignition, becoming less and less as the flame propagated. For example, at TDC 9 out of 100 images could be used to obtain a value for signal ratio.

To calculate the average temperature at each crank angle, the average signal ratios for each image were obtained at each crank angle with the method explained above, and then ensemble-averaged. p_{O2} for each image at each crank angle was obtained by crank angle resolved pressure trace considering 19.1% internally recirculated exhaust gas (Gessenhardt et al. 2015). The ensemble-averaged signal ratios were then used in combination with the ensemble-averaged p_{O2} at that crank angle to calculate the average temperature. The signal ratio images were also converted into temperature images by calculating the temperature for each pixel assuming a constant p_{O2} throughout the field of view. In addition to signal ratios for each image at all crank angles, the mean and standard deviation of pixel values in the ROI were also determined for BG-subtracted red and blue images, and for the signal ratio images.

5 Results

5.1 Anisole versus toluene

For each tracer/fuel mixture, Fig. 11 shows two ensemble-averaged red channel images at − 60 °CA in a typical FOV. The white boundary represents the full FOV, not all of which

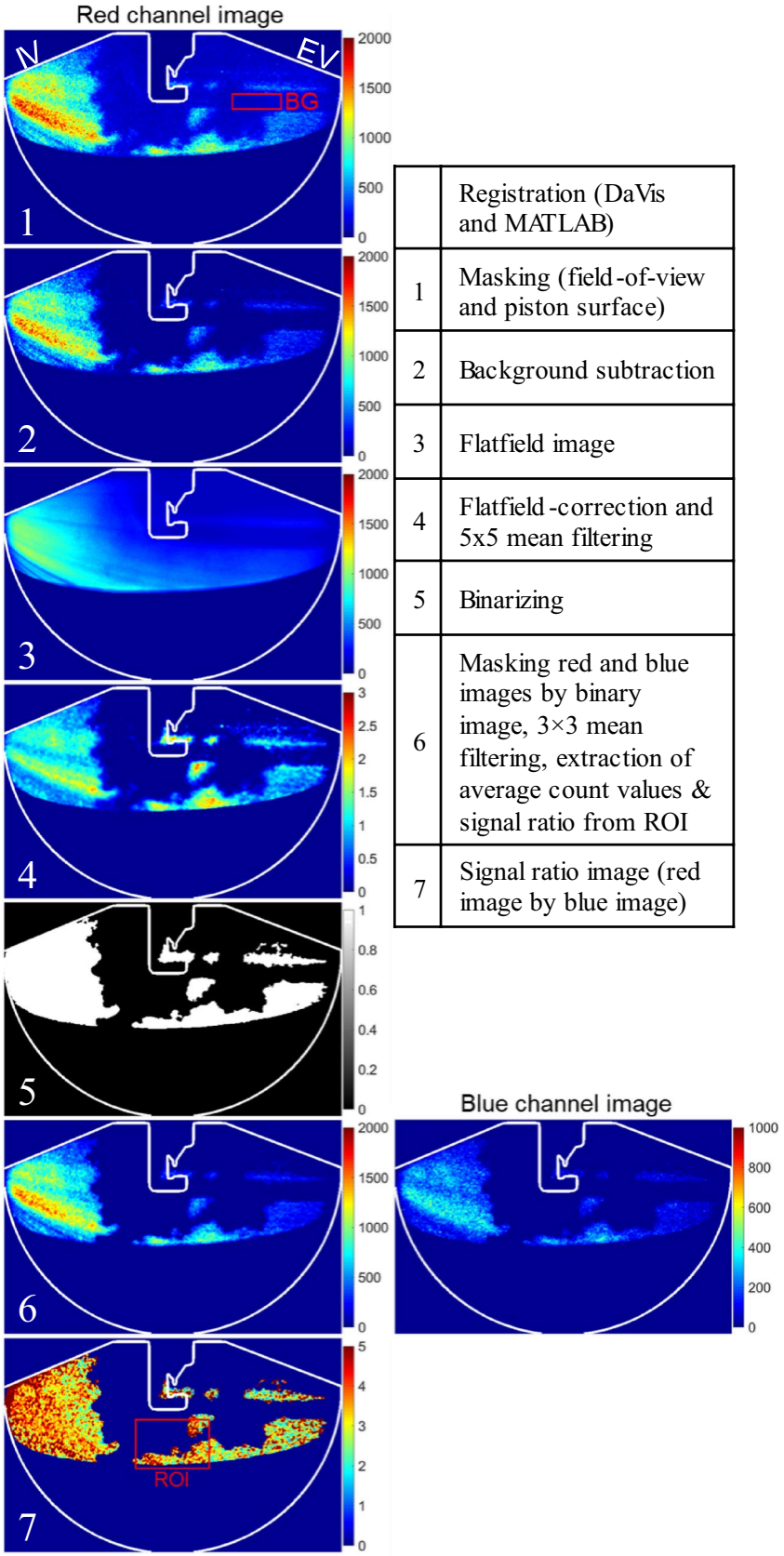

	Registration (DaVis and MATLAB)
1	Masking (field-of-view and piston surface)
2	Background subtraction
3	Flatfield image
4	Flatfield-correction and 5x5 mean filtering
5	Binarizing
6	Masking red and blue images by binary image, 3×3 mean filtering, extraction of average count values & signal ratio from ROI
7	Signal ratio image (red image by blue image)

Fig. 10 Image post-processing steps. The inset shows the post-processing steps applied and the resulting images are numbered accordingly. Intake and exhaust valves are marked as IV and EV, respectively

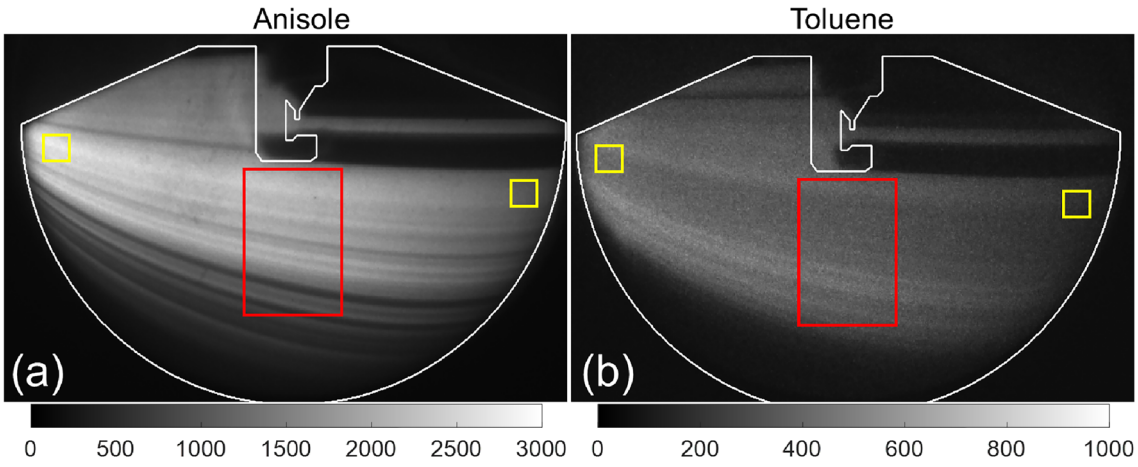

	Anisole (2.5 %)		Toluene (20 %)	
	red	blue	red	blue
Mean counts in ROI	1700	1520	350	780
SNR in ROI	6.8	6.8	3.5	4.5
Change in SNR across the cylinder (% reduction)	60	55	70	65

Fig. 11 LIF images from red channel at −60 °CA at the engine speed of 2000 min^{-1} and 4 bar imep. **a** anisole. **b** toluene. The table lists the average counts in the red square. Red box represents the ROI for mean counts and SNR in ROI. Yellow boxes represent the ROIs to calculate the change in SNR across the cylinder

is illuminated by the laser sheet. The lower boundary of FOV is somewhat dependent on the position of the piston; here, it is below the FOV. The ensembled average counts of 100 images in both channels in a 100 × 150 pixel ROI below the spark plug (red box in Fig. 11) are given in the table below the images. The vertical dimension of ROI is longer than horizontal to compensate for apparent difference in the instantaneous beam profile. The laser energy was similar in both cases. The intensifier gate, gain, and binning were kept the same at 200 ns, 80%, and 2 × 2, respectively. Figure 11 shows that in the red channel, the average detector counts from anisole LIF are ~ 5 times higher than toluene, although the volume of anisole added to isooctane was 8 times less. This can also be attributed to the fact that more of the anisole spectrum is captured in the red channel than in the case of toluene (see Fig. 2). However, the blue channel is matched much better to the toluene spectrum at 475 K, but anisole still has ~ 2 times higher average LIF counts in that channel. The signal-to-noise ratio (SNR) for both tracer/fuel mixture in the ROI (measured in red box) and decrease in SNR across the cylinder (measured by the two yellow boxes across the FOV) are also given in the table below the images in Fig. 11. The average SNR in anisole images is approximately double as compared to that in toluene images. The decrease in SNR is less, but comparable, for anisole images. The similar decrease in SNR confirms that the attenuation is similar for the two tracers, as intended by the difference in concentrations.

Figure 12 shows selected single-shot images from the red channel at crank angles close to compression TDC. The resolution of the imaging system is able to resolve the "stripes" that originate from flaws in the transverse beam profile and from beam steering in the flame front. Anisole LIF images with 2 × 2 binning have approximately 4–5 times higher signal intensity than toluene images with the same binning. Toluene images with 4 × 4 binning show similar intensity as anisole images with 2 × 2 binning, but the resolution of the images is of course worse. Anisole LIF images with 4 × 4 binning also have about four times higher signal intensity than toluene LIF with 4 × 4 binning. With anisole, details in the wrinkled turbulent flame front burning into the mixture can be resolved quite well. Overall, anisole appears to be a good candidate for LIF imaging in low-light applications such as endoscopic engines.

5.2 Temperatures during the compression stroke

Figure 13 shows the temperature progression throughout the compression stroke measured by anisole two-color LIF thermometry using different signal models compared to the adiabatic temperature. The adiabatic temperature was calculated from the crank angle resolved pressure trace with an exponent of $\kappa = 1.4$. This value of κ is used here

for comparison as the measured temperatures should represent the 'core temperature' that is near-adiabatic (Fitzgerald et al. 2010), as opposed to the 'bulk temperature' for which a consolidated value of $\kappa = 1.32$ is used. In the following text, 'adiabatic' refers to this core temperature. The results show that both of the 3D surface fits (with exponential and linear temperature-dependent part) much over-calculated the temperature. The temperature at the start of the compression stroke (− 180 °CA), as calculated by the two-step fit model with a two-parameter exponential temperature-dependent part, is 322.5 K. One approximation to determine the in-cylinder gas temperature at IVC (− 173 °CA) is averaging the temperatures of intake air and cooling water, i.e., 308 K and 380 K (see Table 2), respectively, resulting in an estimated temperature of 344 K, whereas the temperature measured at this crank angle is ~ 325 K. However, since the measured temperature lies within the range of in situ calibration, which was repeated multiple times, it is more likely that the measured temperature is more accurate.

The measured temperature in the first half of the compression stroke is similar for all the investigated models and is in good agreement with the adiabatic temperature. In theory, the measured temperatures should be close to the adiabatic temperature until ignition (− 35 °CA in this case) and will deviate afterward due to additional heat addition from the radiative heat transfer from the flame and additional heating due to pressure rise due to combustion. However, Fig. 13 shows that right after the calibrated range ($p_{O2} = 210$ mbar in this case), the measured temperatures start deviating from the adiabatic temperature, i.e., when the fit function is used for extrapolation instead of interpolation. The degree of deviation is different for each model. However, at ignition the two-step fit models with two- and three-parameter exponential temperature-dependent parts have the lowest deviation (~ 35 K) from the adiabatic temperature, with the two-parameter function being closer to adiabatic temperature before ignition. The 3D surface fit models, although convenient, show a deviation of about 70 and 100 K with exponential and linear temperature-dependent part, respectively.

Because it deviates least from the adiabatic temperature before and at ignition, the two-step fit function with a two-parameter exponential temperature-dependent part was chosen for further evaluation. Figure 14 shows the measured temperature evaluated with this method compared to the adiabatic temperature and SNR for ensemble-averaged red and blue channel images in corresponding colors. The error bars on the measured temperatures represent the cyclic fluctuations in the measured temperature, calculated as the standard deviation of the ROI-averaged temperatures across the ensemble at each crank angle. The temperature fluctuations are small before ignition and start increasing afterward. The SNR is consistent until ignition despite the increase in pressure. This may be attributed to an increase in number density of tracer molecules due to compression. The SNR decreases after ignition, with blue channel image having stronger decrease. The maximum relative error in the measured temperature was found to be less than 3% before the ignition and increased afterward. The reason for the increase in the relative error and the temperature fluctuations after ignition are cyclic variations in flame propagation and low SNR at later crank angles (Peterson et al. 2014). Due to low SNR at − 5 °CA, the measured temperature shows a different trend than the adiabatic temperature. It is likely that if spectroscopic data were available for higher p_{O2} and temperatures, the correlation between temperature, p_{O2}, and signal ratio could be estimated more accurately and the deviation between measured and adiabatic temperature would decrease. Increasing the SNR at later crank angles by increasing the laser energy by introducing a pulse stretcher would also improve the accuracy.

5.3 Temperature distribution in the compression stroke

Figure 15 shows single-shot images of the spatial temperature distribution at different crank angles during the compression stroke. The temperature at the start of the compression stroke is generally uniform throughout the FOV. Some deviations can be seen in the upper left corner close to the intake valve, in some stripes in the lower region, and around the spark plug. These are probably due to remaining errors in the registration procedure. However, these are outside of the ROI used for calculating the mean core temperature at each crank angle. The higher temperature around the spark plug is probably correct since the spark plug would be at a higher temperature and heat transfer may have resulted in higher temperatures close to the spark plug. This is consistent with the work of Kranz et al. (2018). The temperature appears to be more uniform at later crank angles, although the signal-to-noise ratio (SNR) decreases.

5.4 Temperature distribution during gas exchange

Here, the two-color LIF thermometry was utilized to visualize possible temperature stratification during the gas exchange process. Selected single-shot temperature images at different crank angles during the gas exchange process from different cycles are shown in Fig. 16. Here, 360 °CA represents the gas exchange TDC and 380 and 400 °CA represent the intake stroke of the following cycle. The phenomena observed with anisole LIF are consistent with those observed with toluene LIF in previous work on the same test bench by Gessenhardt et al. (2015), in which (via three-pressure analysis) it was determined that at this operating point the combustion efficiency is 97.9%, and that the signals appearing at crank angles late in the exhaust stroke are

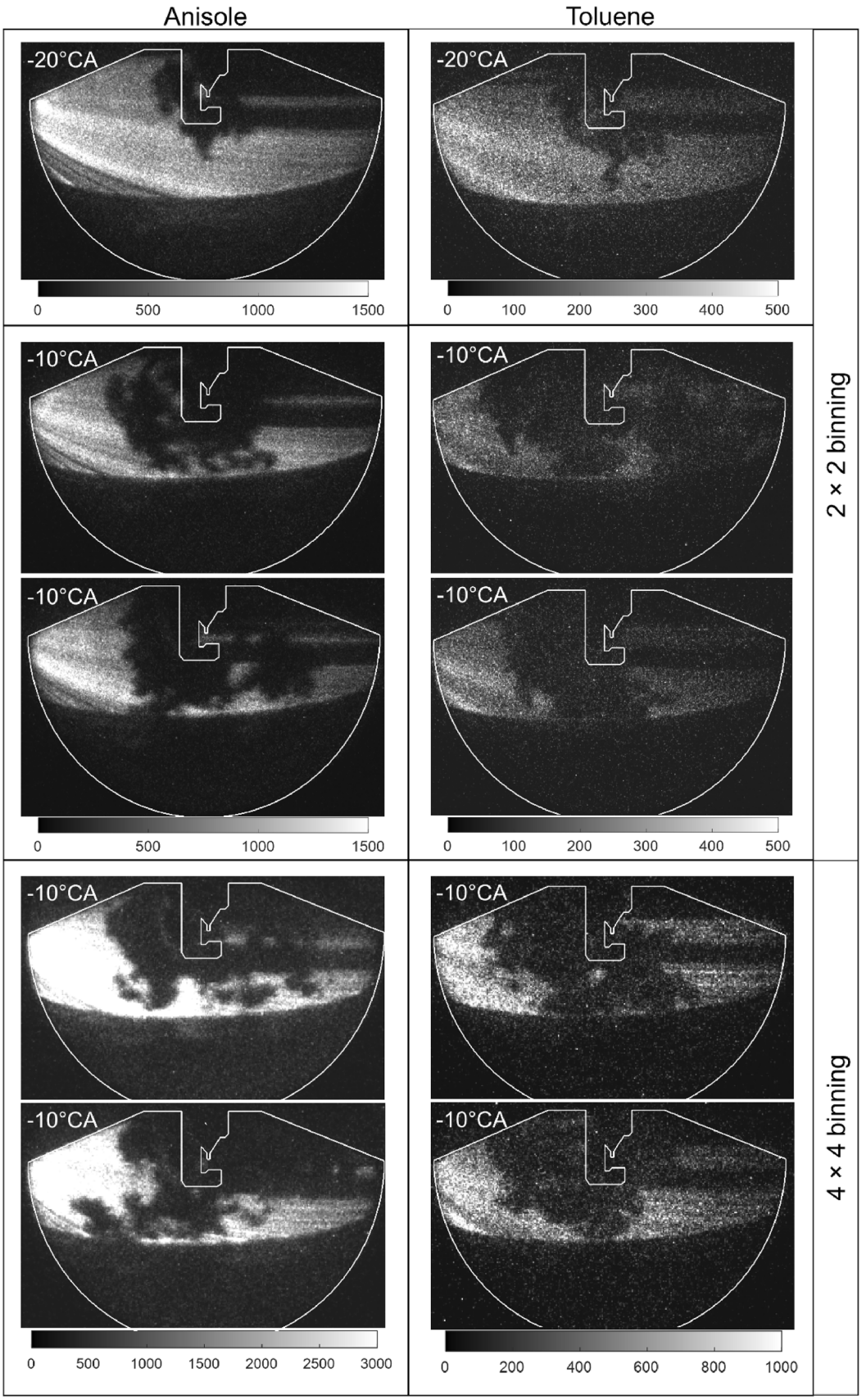
Anisole
Toluene
-20°CA
0 500 1000 1500
-20°CA
0 100 200 300 400 500
-10°CA
0 500 1000 1500
-10°CA
0 100 200 300 400 500
-10°CA
0 500 1000 1500
-10°CA
0 100 200 300 400 500
2 × 2 binning
-10°CA
0 500 1000 1500 2000 2500 3000
-10°CA
0 200 400 600 800 1000
4 × 4 binning

◂**Fig. 12** Single-shot images from the red channel of anisole and toluene LIF at different crank angles and different ICCD binning. Engine speed 2000 min^{-1}, imep = 4 bar, ignition time = − 35 °CA. Anisole LIF images at 4×4 binning are software-binned, and the rest are hardware-binned. Note that the images are on different greyscales, as indicated in the color bars

mostly due to unburnt gases, or other aromatic combustion products with spectral properties similar to those of toluene. Zabeti et al. found that anisole is stable at 930 K, and only 20% decomposed at 1050 K after 1.4 ms (Zabeti et al. 2017). The peak measured temperature based on two-step methods with exponential temperature-dependent parts in this work is under 950 K, which implies that unburnt anisole is still not decomposed. Therefore, the temperatures for the unburnt gases in the gas exchange process were determined assuming that the signals come from unburnt anisole. At 340 °CA, unburnt residuals appear in the region close to the intake valve with temperatures around 450 K, with some cooler regions probably due to small amounts of fresh charge. At 360 °CA, the unburnt residuals appear to move to the right at a slightly higher temperature. At 380 °CA, a clear temperature stratification is observed, with a fresh charge being at a much lower temperature than the exhaust gases ahead. The temperature of the residual gas has increased at this crank angle. The reason for this increase in temperature is backflow of exhaust gases from the still open exhaust valve at this crank angle (Gessenhardt et al. 2015), which are at even higher temperature of 607 K. The fresh charge also appears to be at a higher temperature than the intake air temperature of 308 K (see Table 2), probably because there is conductive heat transfer from the hot engine components and some mixing between residual gases and the fresh charge. At 400 °CA, the temperatures of the 'cooler' fresh charge and 'hotter' residual gases have decreased because more amount of fresh charge has entered the cylinder resulting in overall decrease in temperature. This also supports the accuracy of the temperature measured at BDC (start of compression stroke), since the temperature is showing a decreasing trend toward the temperature of the fresh charge (308 K). Apart from this decrease in temperature caused by fresh charge, additional cooling can be expected from the gas expansion due to lower pressures in the cylinder during the throttled intake stroke.

6 Conclusions

Anisole, due to its photophysical properties, is a strong candidate for use as a tracer in non-intrusive LIF diagnostics in combustion engines and other applications. Here, it was used as a tracer with the base fuel isooctane in an all-metal engine with endoscopic access. Imaging in two spectral portions of

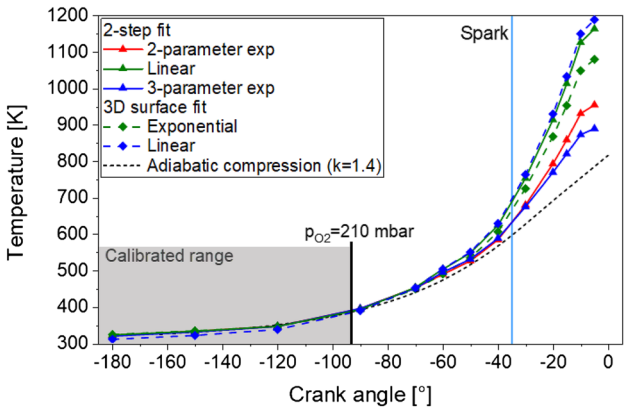

Fig. 13 Temperature in the compression stroke with various signal models compared to the adiabatic temperature. The legend entries describe the temperature-dependent part of the signal models. The p_{O2}-dependent part of all signal models was same as in equation (2)

anisole fluorescence was performed with two ICCD cameras through a UV endoscope system. Anisole LIF signal levels were first compared to those of toluene. Toluene is one of the best-characterized tracers, but anisole yielded higher signal levels when both tracers' concentration was limited by laser attenuation, which here was the case for 20% toluene vs. 2.5% anisole. The anisole signal was ~ 5 times higher in the spectral range of 320 ± 20 nm with 8 times less concentration at − 60 °CA (before TDC during compression stroke). Small structures of the turbulent flame burning into the anisole/isooctane mixture were clearly visible after ignition.

Since this test was promising, anisole was used for ratiometric two-color LIF thermometry, a technique we had implemented endoscopically before with toluene, but mostly without achieving reasonable quality single-shot images

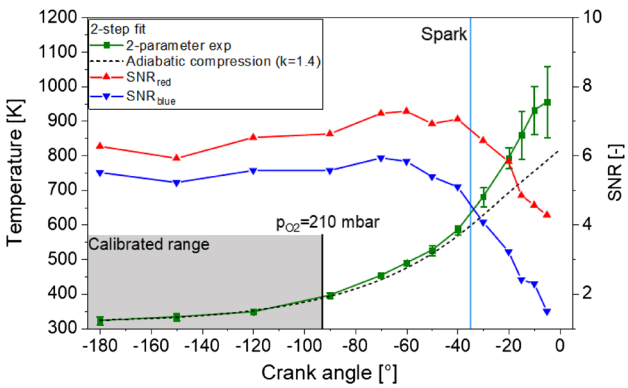

Fig. 14 Measured temperature evaluated with two-step fit model with two-parameter exponential temperature-dependent part. The points on the green line show the mean measured temperature, and the error bars show the standard deviation over the 100 images. Red and blue lines are the SNR for ensemble-averaged red and blue images at each crank angle

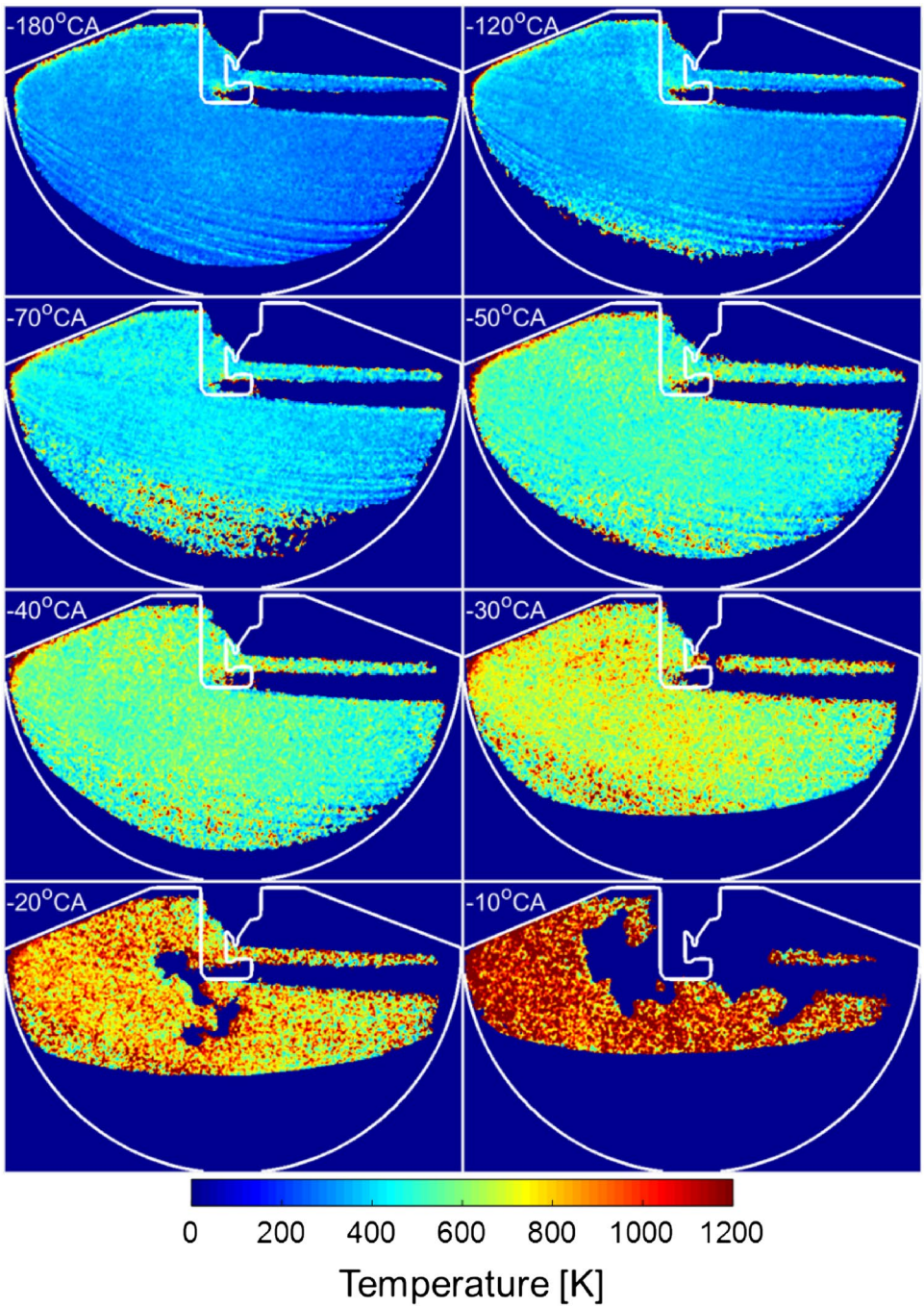

Fig. 15 Selected single-shot temperature images at different crank angles during the compression stroke from different cycles

(Gessenhardt et al. 2015). From spectroscopic data in the literature, different empirical signal models considering the effects of temperature and oxygen partial pressure (p_{O2}) were assembled. The models can be categorized mainly as two-step fit function, fitting separately for p_{O2} and temperature, and a single 3D surface fit function incorporating the effect of both parameters on the signal ratio. Each category had further variations in terms of the function governing the effect of temperature on the signal ratio. An in situ calibration was performed in nitrogen and air at temperatures ranging from room temperature to 573 K. The calibrated models were used to convert the red/blue LIF signal ratio to temperature in the compression stroke, which was compared to the adiabatic pressure-based temperature. It was found that the 3D-surface fit functions greatly overestimated the temperatures in the late compression stroke. The two-step fit functions with a two-parameter exponential temperature-dependent part yielded temperatures closer to the adiabatic temperature until ignition, but with some deviation when the p_{O2} in the cylinder increased beyond that in available

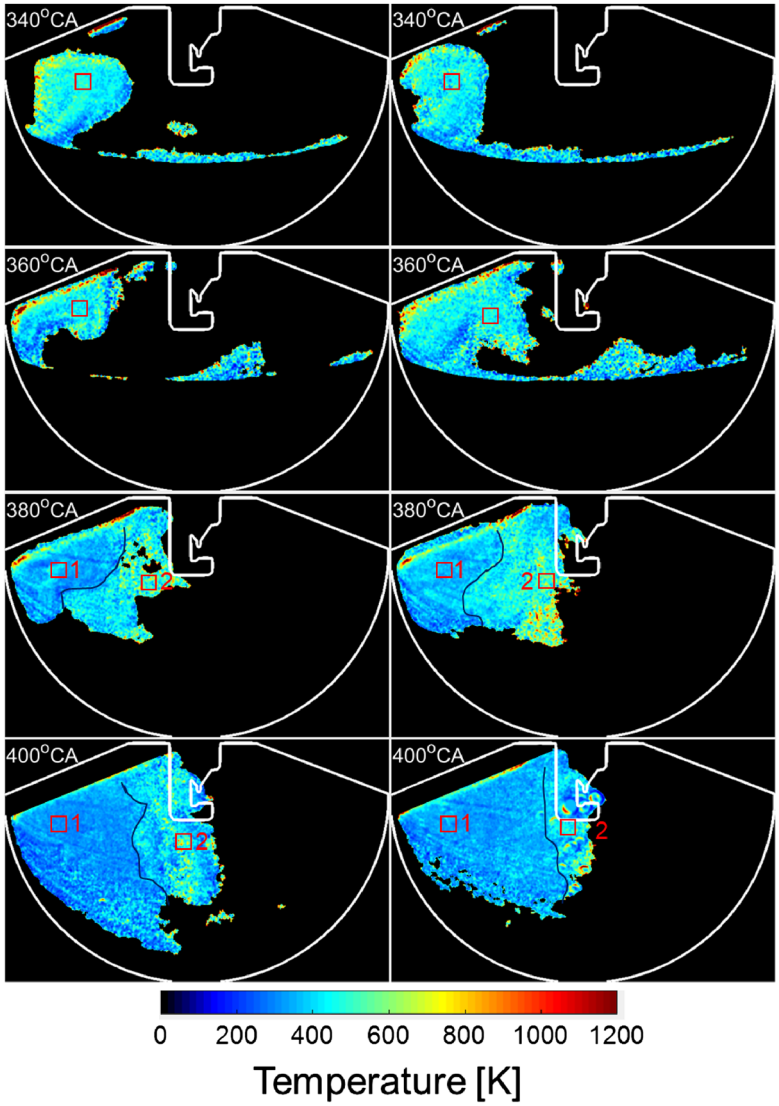

Temperature	
Image 1	Image 2
441 K	449.8 K
451.3 K	451.8 K
ROI1: 384.5 K ROI2: 510.5 K	ROI1: 370 K ROI2: 510.8 K
ROI1: 335.6 K ROI2: 420.8 K	ROI1: 333.8 K ROI2: 433.98 K

Fig. 16 Selected single-shot spatial temperature distribution during gas exchange process from different cycles. The red squares represent the ROIs from which the temperatures listed in the table on the right were determined. The dark blue lines represent the apparent boundary between the fresh charge and the residual unburnt gas from the previous cycle

spectroscopic data and the effect of increasing p_{O2} on the signal ratio was extrapolated.

The two-step fit function with a four-parameter exponential temperature-dependent part was then used to visualize the spatial temperature distribution at different crank angles during the compression stroke. As expected for port fuel-injected operation, the temperature was found to be mostly uniform across the FOV, with later crank angles showing more noise because of lower signal due to the fluorescence lower quantum yield at higher temperatures and pressure. The spatial temperature distribution around the gas exchange TDC were also visualized. The residual gas was assumed to be unburnt anisole containing fuel. The residual gas mixture was observed moving along the in-cylinder tumble at crank angles shortly before TDC with measured temperatures close to the temperature measured in the exhaust downstream of the valve. Clear temperature segregation was observed when fresh charge started entering the cylinder with temperature decreasing with progressing intake stroke, consistent with what was observed in our previous work with toluene LIF (Gessenhardt et al. 2015).

The results showed that for anisole LIF two-color thermometry considering the effect of oxygen partial pressure is

also important. In this respect, the lack of spectroscopic data is an issue, since the available data only cover about 7% of the range encountered in p_{O2}. If further spectroscopic data were available, the accuracy of the temperature determined by two-color thermometry with anisole may be improved. The correlation of signal ratio and temperature also needs to be more accurately established with the help of more spectroscopic data, especially at high temperatures. The available data covered more than 50% of the required temperature range, but inaccurate extrapolation nevertheless may result in inaccuracies at high temperatures.

Supplementary Information The online version contains supplementary material available at https://doi.org/10.1007/s00348-023-03733-5.

Acknowledgements The author would like to thank DAAD and the Higher Education Commission of Pakistan for sponsoring the work of M.A.S. In addition, we thank Dr. Martin Goschütz and Sadik Sheik for helping with the experiments and providing valuable input. We acknowledge support by the Open Access Publication Fund of the University of Duisburg-Essen.

Author contributions MAS contributed to conceptualization, data collection, data analysis, and writing original draft; SJ performed data analysis, figure preparation, and review and editing; SAK performed data analysis, review and editing, and supervision.

Funding Open Access funding enabled and organized by Projekt DEAL. The Author MAS was funded by Higher Education Commission of Pakistan under human resource development initiative for universities of engineering sciences and technologies in Pakistan (Grant Number: 50020962).

Availability of data and materials Data will be made available upon reasonable request.

Declarations

Conflict of interest The authors declare no competing interests.

Ethical approval Not applicable.

References

Alger T, Huang Y, Hall M, Matthews RD (2001) Liquid film evaporation off the piston of a direct injection gasoline engine. SAE Tech Paper. https://doi.org/10.4271/2001-01-1204

Attar MA, Zhao H, Herfatmanesh MR, Cairns A (2015) Turbulent flame boundary and structure detection in an optical DISI engine using tracer-based two-line PLIF technique. Exp Thermal Fluid Sci 68:545–558. https://doi.org/10.1016/j.expthermflusci.2015.06.015

Bakenhus M, Reitz RD (1999) "Two-color combustion visualization of single and split injections in a single-cylinder heavy-duty D.I. diesel engine using an endoscope-based imaging system. SAE Tech Paper. https://doi.org/10.4271/1999-01-1112

Benzler T (2019) Photo-physical characterization of aromatic compounds for laser-induced fluorescence based diagnostics of fuel concentration, temperature, and equivalence ratio in practical combustion processes. PhD thesis, University of Duisburg-Essen, Duisburg

Bladh H, Brackmann C, Dahlander P, Denbratt I, Bengtsson PE (2005) Flame propagation visualization in a spark-ignition engine using laser-induced fluorescence of cool-flame species. Meas Sci Technol 16(5):1083–1091. https://doi.org/10.1088/0957-0233/16/5/006

Burkardt P et al (2021) Toward co-optimization of renewable fuel blend production and combustion in ultra-high efficiency SI engines. Int J Engine Res 24(1):29–41. https://doi.org/10.1177/14680874211040995

Deguchi Y et al (2002) Industrial applications of temperature and species concentration monitoring using laser diagnostics. Meas Sci Technol 13(10):103–115. https://doi.org/10.1088/0957-0233/13/10/201

Dierksheide U, Meyer P, Hovestadt T, Hentschel W (2002) Endoscopic 2D particle image velocimetry (PIV) flow field measurements in IC engines. Exp Fluids 33(6):794–800. https://doi.org/10.1007/s00348-002-0499-3

Drake MC, Fansler TD, Solomon AS, Szekely GA (2003) Piston fuel films as a source of smoke and hydrocarbon emissions from a wall-controlled spark-ignited direct-injection engine. SAE Tech Paper. https://doi.org/10.4271/2003-01-0547

Düwel I, Kunzelmann T, Schorr J, Schulz C, Wolfrum J (2003) Application of fuel tracers with different volatilities for planar LIF/Mie drop sizing in evaporating systems. In: Proceedings of the 9th International Conference on Liquid Atomization and Spray Systems ICLASS, Sorrento, Italy

Eicheldinger S, Karmann S, Prager M, Wachtmeister G (2021) Optical screening investigations of backfire in a large bore medium speed hydrogen engine. Int J Engine Res 23(5):893–906. https://doi.org/10.1177/14680874211053171

Eismark J, Balthasar M, Karlsson A, Benham T, Christensen M (2009) Role of late soot oxidation for low emission combustion in a diffusion-controlled, high-EGR, heavy duty diesel engine. SAE Tech Paper. https://doi.org/10.4271/2009-01-2813

Etikyala S, Koopmans L, Dahlander P (2022) Visualization of soot formation in load transients during GDI engine warm-up. Int J Engine Res 24(7):3073–3084. https://doi.org/10.1177/14680874221141125

Fach C, Rödel N, Schorr J, Krüger C, Dreizler A, Böhm B (2021) Multi-parameter imaging of in-cylinder processes during transient engine operation for the investigation of soot formation. Int J Engine Res 23(9):1573–1585. https://doi.org/10.1177/14680874211019976

Fach C, Rödel N, Schorr J, Krüger C, Dreizler A, Böhm B (2022) Investigation of in-cylinder soot formation in a DISI engine during transient operation by simultaneous endoscopic PIV and flame imaging. Int J Engine Res 24(3):1175–1189. https://doi.org/10.1177/14680874221079764

Faust S, Dreier T, Schulz C (2013) Photo-physical properties of anisole: temperature, pressure, and bath gas composition dependence of fluorescence spectra and lifetimes. Appl Phys B Lasers Opt 112(2):203–213. https://doi.org/10.1007/s00340-013-5420-7

Faust S, Goschütz M, Kaiser SA, Dreier T, Schulz C (2014) A comparison of selected organic tracers for quantitative scalar imaging in the gas phase via laser-induced fluorescence. Appl Phys B Lasers Opt 117(1):183–194. https://doi.org/10.1007/s00340-014-5818-x

Faust S (2013) Characterisation of organic fuel tracers for laser-based quantitative diagnostics of fuel concentration, temperature, and equivalence ratio in practical combustion processes. In; PhD thesis, University of Duisburg-Essen, Duisburg

Fitzgerald RP, Steeper R, Snyder J, Hanson R, Hessel R (2010) Determination of cycle temperatures and residual gas fraction for HCCI negative valve overlap operation. SAE Int J Engines 3(1):124–141

Frieden D, Sick V (2003) Investigation of the fuel injection, mixing and combustion processes in an SIDI engine using quasi-3D LIF imaging. SAE Trans 724:270–281

Fuyuto T, Kronemayer H, Lewerich B, Koban W, Akihama K, Schulz C (2006) Laser-based temperature imaging close to surfaces with toluene and NO-LIF. J Phys Conf Ser 45:69–76. https://doi.org/10.1088/1742-6596/45/1/010

Geiler JN, Grzeszik R, Quaing S, Manz A, Kaiser SA (2017) Development of laser-induced fluorescence to quantify in-cylinder fuel wall films. SAE Int J Engine Res 19(1):134–147. https://doi.org/10.1177/1468087417733865

Gessenhardt C (2013) Endoskopische Bestimmung des Temperaturfeldes im Brennraum eines Ottomotors mittels laserinduzierter Fluoreszenz. In: PhD thesis, University of Duisburg-Essen, Duisburg

Gessenhardt C, Schulz C, Kaiser SA (2015) Endoscopic temperature imaging in a four-cylinder IC engine via two-color toluene fluorescence. Proc Combust Inst 35(3):3697–3705. https://doi.org/10.1016/j.proci.2014.06.085

Hochgreb S (2001) Liquid fuel impingement on the piston bowl of a direct-injection, spark-ignited (DISI) engine under stratified operation. SAE Tech Paper. https://doi.org/10.4271/2001-01-3646

Hult J, Mayer S (2013) A methodology for laser diagnostics in large-bore marine two-stroke diesel engines. Meas Sci Technol. https://doi.org/10.1088/0957-0233/24/4/045204

James VS, Smith D (2005) Crank-angle resolved imaging of fuel distribution, ignition and combustion in a direct-injection spark-ignition engine. SAE Trans 114:1575–1585

Karmann S, Eicheldinger S, Prager M, Wachtmeister G (2022) Optical and thermodynamic investigations of a methane and hydrogen blend fueled large bore engine. Int J Engine Res 23(5):846–864. https://doi.org/10.1177/14680874211066735

Koban W, Koch JD, Hanson RK, Schulz C (2005) Oxygen quenching of toluene fluorescence at elevated temperatures. Appl Phys B Lasers Opt 80(6):777–784. https://doi.org/10.1007/s00340-005-1769-6

Kuwahara K, Ando H (2000) Diagnostics of in-cylinder flow, mixing and combustion in gasoline engines. Meas Sci Technol 11(6):95–111. https://doi.org/10.1088/0957-0233/11/6/202

Luong M, Zhang R, Schulz C, Sick V (2008) Toluene laser-induced fluorescence for in-cylinder temperature imaging in internal combustion engines. Appl Phys B Lasers Opt 91(3–4):669–675. https://doi.org/10.1007/s00340-008-2995-5

Miers SA, Ng H, Ciatti SA, Stork K (2005) Emissions, performance, and in-cylinder combustion analysis in a light-duty diesel engine operating on a fischer-tropsch, biomass-to-liquid fuel. SAE Techn Paper. https://doi.org/10.4271/2005-01-3670

Kranz P et al (2018) In-cylinder LIF imaging, IR-absorption point measurements, and a CFD simulation to evaluate mixture formation in a CNG-fueled engine. SAE Tech Paper. https://doi.org/10.4271/2018-01-0633

Peterson B, Baum E, Böhm B, Sick V, Dreizler A (2013) High-speed PIV and LIF imaging of temperature stratification in an internal combustion engine. Proc Combust Inst 34(2):3653–3660. https://doi.org/10.1016/j.proci.2012.05.051

Peterson B, Baum E, Böhm B, Sick V, Dreizler A (2014) Evaluation of toluene LIF thermometry detection strategies applied in an internal combustion engine. Appl Phys B 117(1):151–175. https://doi.org/10.1007/s00340-014-5815-0

Reichle R, Pruss C, Gessenhardt C, Schulz C, Osten W (2012) Diffractive/refractive (hybrid) UV-imaging system for minimally invasive metrology: design, performance, and application experiments. Appl Opt 51(12):1982–1996. https://doi.org/10.1364/AO.51.001982

Richter M, Axelsson B, Aldén M (1998) Engine diagnostics using laser induced fluorescence signals collected through an endoscopic detection system. SAE Tech Paper. https://doi.org/10.4271/982465

Schulz C, Sick V (2005) Tracer-LIF diagnostics: quantitative measurement of fuel concentration, temperature and fuel/air ratio in practical combustion systems. Prog Energy Combust Sci 31(1):75–121. https://doi.org/10.1016/j.pecs.2004.08.002

Schulz F, Samenfink W, Schmidt J, Beyrau F (2016) Systematic LIF fuel wall film investigation. Fuel 172:284–292. https://doi.org/10.1016/j.fuel.2016.01.017

Schulz F, Beyrau F (2018) Systematic investigation of fuel film evaporation. SAE Tech Paper. https://doi.org/10.4271/2018-01-0310

Sczomak DP, Zhao A, Simon MS, Zeng Y (2010) High speed endoscope imaging to supplement CFD analysis and combustion testing for sidi engine startup development. SAE Tech Paper. https://doi.org/10.4271/2010-01-0347

Sementa P, Maria Vaglieco B, Catapano F (2012) Thermodynamic and optical characterizations of a high performance GDI engine operating in homogeneous and stratified charge mixture conditions fueled with gasoline and bio-ethanol. Fuel 96:204–219. https://doi.org/10.1016/j.fuel.2011.12.068

Shahbaz MA (2021) Endoscopic imaging techniques for gas phase temperature, combustion, fuel films, and soot in internal combustion engines. In: PhD thesis, University of Duisburg-Essen, Duisburg

Shahbaz MA, Kaiser SA, Schütte M, Berg T (2023) Characterization of different endoscopic imaging systems in ultraviolet range for combustion applications. Appl Optics. https://doi.org/10.1364/ao.489440

Shiozaki T, Nakajima H, Kudo Y, Miyashita A, Aoyagi Y (1996) The analysis of combustion flame under EGR conditions in a dl diesel engine. SAE Trans 105:396–409

Smith JD, Sick V (2005) High-speed fuel tracer fluorescence and OH radical chemiluminescence imaging in a spark-ignition direct-injection engine. Appl Opt 44(31):6682–6691. https://doi.org/10.1364/AO.44.006682

Tran KH, Morin C, Kühni M, Guibert P (2013) Fluorescence spectroscopy of anisole at elevated temperatures and pressures. Appl Phys B Lasers Opt 115(4):461–470. https://doi.org/10.1007/s00340-013-5626-8

Warey A, Huang Y, Matthews RD, Hall M, Ng H (2002) Effects of piston wetting on size and mass of particulate matter emissions in a DISI engine. SAE Tech Paper. https://doi.org/10.4271/2002-01-1140

Witzel B (2007) Konstruktion optischer Zugänge an einem 4-Zylinder Serienmotor zur Durchführung laseroptischer Messungen mittels mikroinvasiver Endoskoptechnik. In: Bachelor thesis, University of Duisburg-Essen, Duisburg

Zabeti S, Aghsaee M, Fikri M, Welz O, Schulz C (2017) Optical properties and pyrolysis of shock-heated gas-phase anisole. Proc Combust Inst 36(3):4525–4532. https://doi.org/10.1016/j.proci.2016.06.156

Zimmermann F (2006) New approaches for optical and microoptical diagnostics in IC engines. In: PhD thesis, Ruprecht-Karls-Universität, Heidelberg, November